Mandible Bone Osteoporosis Detection using Cone-beam Computed Tomography

Rasha F. Abu Marar
Department of Computer Science
Faculty of Information Technology
Middle East University
Amman, Jordan
ramarar82@gmail.com

Diaa M. Uliyan
Department of Information Computer Science
College of Computer Science and Engineering
University of Hai'l
Hai'l, Saudi Arabia
d.uliyan@uoh.edu.sa

Hamza A. Al-Sewadi
Department of Computer Science
Faculty of Information Technology
Middle East University
Amman, Jordan
hsewadi@meu.edu.jo

***Abstract*-Osteoporosis is a common health problem that affects one-third of women over the age of 50 and it may not be detected until bone fractures occur. Osteoporosis is low bone mass and microarchitectural deterioration of bone tissue, which affects bone fragility and raises fracture risks. Early mandible bone osteoporosis detection could help reduce the risk of jaw fracture and dental implant failure. To solve this problem, a diagnostic algorithm for automatic detection of osteoporosis in Cone-Beam Computed Tomography (CBCT) images is presented and 120 mandible CBCT images of 50-85 year-old women have been utilized. These images are classified into two classes: normal and osteoporotic. Their classification is based on the T-score which derives from the Dual-Energy X-ray Absorptiometry (DEXA). The proposed algorithm consists of image processing, feature extraction, and Artificial Neural Network (ANN) classification. Images are segmented and edges are detected. Then, texture features are extracted from the segmented regions. Finally, a feed-forward back-propagation ANN classifier is employed. Seven parameters were involved in the experiment data preparation as input: coarseness, contrast, direction, number of edges, length of edges, mean length of edges, and the number of edge pixels. The results demonstrate the effectiveness of the proposed method. With the help of the proposed method, dentists will be able to predict osteoporosis accurately and efficiently without the need for further examination since CBCT has been widely accepted in dentistry and the dentist is the most common health care professional that elderly visit regularly.**

Keywords-artificial intelligence; neural network classifiers; osteoporosis; cone-beam CT; image processing

I. INTRODUCTION

Osteoporosis is the decreased bone mass and microarchitectural deterioration of the bone scaffold, leading to bone fragility and enhanced susceptibility to fractures [1, 2]. The golden standard measurement of Bone Mass Density (BMD), or aspects related to bone structure is DEXA [3]. Osteoporosis is common in the elderly whereas the dentist is often the only healthcare professional that they visit regularly. In dentistry, early detection is important as patients with osteoporosis may suffer from high risk of jaw fracture. Cone-Beam Computed Tomography (CBCT) has been widely accepted in dentistry since its introduction in 1998 [4]. Current CBCT devices do not produce grey-scale values not a calibrated Housefield Unit (HU) values. However, the values differ for different devices as well as on the object placement in the imaged Field of View (FOV) [5].

Despite the ability to detect bone density and the quality of structures, some studies have been conducted on the use of HU values in detecting osteoporosis [6, 7]. Authors in [8] used the evaluation of alveolar bone changes as a valuable predictor for osteoporosis. Mandibular Cortical Index (MCI), Mandibular Computed Tomography (MCT), Mental Index (MI), and bone loss were assessed from the radiographs. No significant relationship was found in the MI between the right and the left side at the mental foramen region, and a statistical significance between MI and MCI was reported. Authors in [9] found a strong correlation coefficient accuracy in predicting osteoporosis in the lumbar vertebrae and the femoral neck. There finding should be confirmed on other CBCT devices, and the cervical vertebrae which rarely appears in CBCT for dental matters. Authors in [10] evaluated the validity of CBCT for assessing mandibular bone quality using the Klemetti classification which was not adequate means of assessing bone quality with CBCT. Authors in [11] determined the region of interest (RoI) of the condyle mandibular as a biomarker for feature extraction and classification of bone conditions. Bone Mineral Density (BMD) was classified in two classes, normal

Corresponding author: Diaa M. Uliyan

and abnormal with results with 88.0% accuracy and 88.0% sensitivity. Authors in [12] found that there is no relationship between the right and the left side at the mental foramen region. Also, there was a statistical significance between MI and MCI. Authors in [13] observed a positive correlation of spine BMD in the right and left mandibular CT values and HU measurements. The study didn't conclude an accurate unique value for detecting osteoporosis. Authors in [3] found that it is possible to predict the osteoporosis through the Radiographic Density (RD) related to the body of C2 and the left lateral mass of C1 more accurately than from other areas. The techniques are strict and hard to implement and the study didn't conclude to an accurate unique value for osteoporosis detection. Authors in [14] found that the risk of osteoporosis is significantly affected by the bone density of mandibular condyle, age, and gender. Each of the discussed above studies achieved a certain goal, but did not conclude to an accurate value to surely detect osteoporosis from mandible CBCT without the need of a DEXA scan.

This approach intends to design and implement image analysis and AI algorithms in order to specify feature values in CBCT with the main purpose of detecting osteoporosis, by selecting mandibular RoIs from CBCT images. The images are enhanced by processing on all RoIs followed by segmentation and feature extraction. These features are the potential features of the osteoporosis predictor. Finally, the selected features will be used as input for classifying the patients into two classes (healthy or osteoporotic) using Back Propagation Artificial Neural Networks (ANNs).

II. PROPOSED METHOD

The algorithm proposed in this paper is designed for automatic detection of osteoporosis in CBCT images. The system consists of six steps: (a) Input the DICOM image, (b) Image Preprocessing, (c) Extraction of image features, (d) Recognition using ANN classifier, (e) Detection of osteoporosis. Figure 1 shows the overall system architecture.

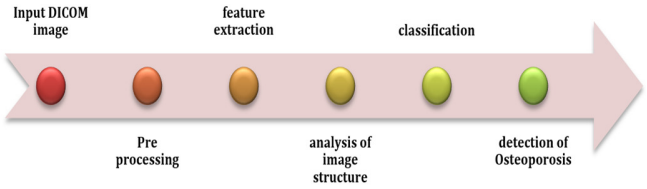

Fig. 1. Architecture of the proposed algorithm.

A. Input Image

Image acquisition is the process of obtaining a mandible slice were both foramina appear simultaneously on the coronal views (the green line in Figure 2). This is checked by navigating through all the CBCT image slices.

B. Image Preprocessing

Image preprocessing is a required preparatory step to ensure the high accuracy of the subsequent steps. Preprocessing becomes necessary because most of real life data are noisy, inconsistent, and incomplete [15]. Preprocessing in a bone image is a crucial initial step before texture analysis is performed. DICOM images pass through the preprocessing steps which include noise removal and the elimination of redundant information as much as possible. Images were taken from a CS8100 3D machine, 75kvp and 4mAs. Figure 3 shows the block diagram of image preprocessing. This sub section describes the steps of image preprocessing.

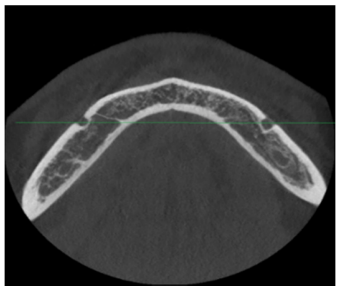

Fig. 2. Mandible slice with both foramina appearing simultaneously.

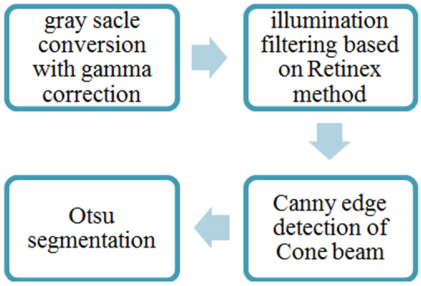

Fig. 3. Block diagram of image pre-processing steps.

1) Gray Scale Image Conversion

In image recognition applications such as medical image analysis, it is common to convert the input images to grayscale since grayscale features have a good impact on recognition performance. The considered images in the proposed method are grayscale images. The method starts by reading an indexed mandible image I with RGB color map and converts it to a grayscale color map image by removing the hue and saturation features while retaining the luminance. The conversion function g_s takes a I^{NxMx3} color image and converts it to a I^{NxM} representation. R values are assumed to be [0-1]. R, G, and B channels represent linear without gamma corrected features. The function is defined as follows:

$$g_{Luminance} = 0.3\, I_R + 0.95\, I_G + 0.11\, I_B \quad (1)$$

Here, *Luminance* is the standard algorithm where it is implemented by MATLAB's rgb2gray() function. To enhance the gamma from the image due to light inconsistency in the image, the equation can be rewritten as follows:

$$g_{lightness} = {}^{1}/_{100}\,(116 * f(y) - c) \quad (2)$$

The function $g_{lightness}$ is a nonlinear transformation [16] which increases the *Lightness* to be more closely related to human perception. In our experiments c=16. $f(y)$ is defined as:

$$y = 0.2126\, I_R + 0.7152\, I_G + 0.0722\, I_B \quad (3)$$

and

$$f(y) = \begin{cases} y^{\frac{1}{3}}, \ y > (\frac{6}{29})^3 \\ \frac{1}{3} * \left(\frac{29}{6}\right)^2 * y + \frac{4}{29}, \ otherwise \end{cases} \quad (4)$$

As a result, the image $f(y)$ is a normalized *Lightness* image in the range [0-1].

2) Filtering

Acquired medical images' visibility is often affected by light scattering. In order to detect and remove poor visibility in cone beam images, filtering process has an effective method for visibility enhancement from a single gray cone beam image. Visibility enhancement techniques of degraded images are classified into three main classes: histogram equalization [17], discrete wavelet transform [18] and Retinex method [19, 20]. The Retinex method was developed in [20] and relies on the fact that color saturation has little or no correspondence with luminance variation. Retinex is a well-known method used in image enhancement. It analyzes the illumination reflectance model of image via the following equation:

$$I(x,y) = L(x,y)\, R(x,y) \quad (5)$$

where I is the gray scale image, L is the illumination and R is the reflectance of point lines in (x, y) position. The goal of the Retinex method is to eliminate the L while retaining the reflectance component R. It improves the low-contrast images of typical poor visibility conditions via the mathematical equation:

$$R(x,y) = Log\, I(x,y) - Log\, F(x,y) * I(x,y) \quad (6)$$

where $R(x, y)$ represents the Retinex, $I(x, y)$ is the image distribution and '$*$' is the convolution operator. $F(x,y) = Ke^{-(x^2+y^2)/c^2}$ is the Gaussian function with c being a constant equal to 16. A small value of c results in a narrower surround. K is selected such that $\iint F(x,y)\, dx\, dy = 1$. The result of filtering would be like the example shown in Figure 4.

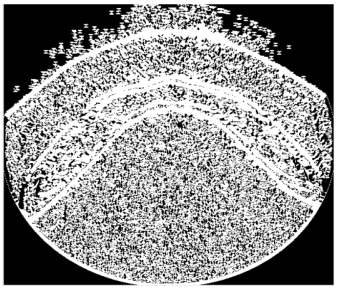

Fig. 4. Image after filtering.

3) Canny Edge Detection

Canny edge detection is a standard edge detection technique. Since its creation by John Canny at MIT in 1983, it still outperforms many newer algorithms [21]. The algorithmic steps for canny edge detection technique are:

- Smooth image $f(r, c)$ with a 5×5 Gaussian filter as given by:

$$G'(x,y) = I(x,y) * G(x,y) \quad (7)$$

where $G(x,y) = \frac{1}{2\,\pi\sigma^{\,2}} e^{-\frac{x^2}{2\sigma^2}}$ is the Gaussian function with $\sigma = [1-6]$.

- Get the first derivatives in horizontal (G_x) and vertical direction (G_y). From these two images, we can find edge gradient and direction for each pixel as follows:

$$G_{\,edge\ gradient} = \sqrt{G_x^2 + G_y^2} \quad (8)$$

and

$$G_{\,direction} = tan^{-1}(\frac{G_y}{G_x}) \quad (9)$$

Gradient direction is always perpendicular to the edges. It is rounded to one of four angles representing vertical, horizontal and two diagonal directions.

- Apply non-maximal or critical suppression to the gradient magnitude.
- Apply threshold to the non-maximal suppression image [22].

Figure 5 shows the image of Figure 1 after applying Canny edge detection.

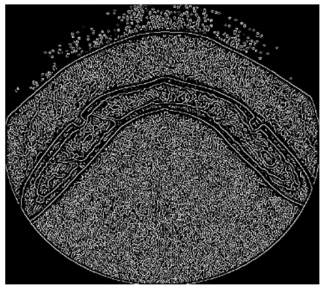

Fig. 5. Image after Canny edge detection.

4) Segmentation

Image segmentation is the process of partitioning a digital image into multiple regions or sets of pixels.

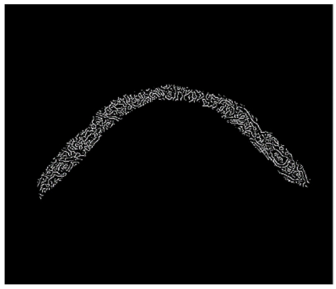

Fig. 6. The segmented mandible image.

We employed a segmentation method based on image histogram projection and Otsu threshold [23] to produce a set of regions that cover the entire mandible bone image and a set of contours extracted from the image. After digitally segmenting the image to extract the inner trabecular bone, it will look like the one illustrated in Figure 6, where only the

RoI for the test is left, while all outer region pixels are removed. The basic idea of Otsu thresholding is examining the optimal or several optimal grayscale values for splitting the inner trabecular bone as RoI in a mandible bone image from the background based on their grayscale histograms. The histogram of the image I with size $N \times M$ is calculated using two main features: the gray level of a pixel $f(x,y)$ and its local average gray level:

$$g(x,y) = \frac{1}{NM}\sum_{i=0}^{L}\sum_{j=0}^{L} f(x+i, y+j).$$

The histogram of the image is defined using probability measure as follows:

$$p_{ij} = \frac{r_{ij}}{NxM} \quad (10)$$

where r_{ij} is the total number of occurrence of image points (i,j) in image I, and $i, j = 0, 1, \ldots, L\text{-}1$. Here, L represents the number of divergent gray scales and $\sum_{i=0}^{L-1}\sum_{j=0}^{L-1}(p_{ij}) = 1$. The pixels in the image are classified into two main classes *C0* and *C1* to represent background and objects respectively via probabilities of class occurrence ω and class means μ as follows:

$$class\ 1 \rightarrow \omega_0(s,t) = \sum_{i=0}^{s-1}\sum_{j=0}^{t-1} p_{ij} \quad (11)$$

$$class\ 2 \rightarrow \omega_1(s,t) = \sum_{i=0}^{s-1}\sum_{j=0}^{t-1} p_{ij} \quad (12)$$

where s and t are threshold values determined from image histogram, i.e. s=maximum (gray scale values), t=maximum (local average gray scale values). The intensity mean value vectors of the two classes and the total mean vector can be expressed as follows:

$$\mu_0(\mu_{00}, \mu_{01})^T = \left[\sum_{i=0}^{s-1}\frac{f(x,y)*p_{ij}}{\omega_0}, \sum_{j=0}^{t-1}\frac{g(x,y)*p_{ij}}{\omega_0}\right]^T \quad (13)$$

$$\mu_1(\mu_{10}, \mu_{11})^T = \left[\sum_{i=0}^{s-1}\frac{f(x,y)*p_{ij}}{\omega_1}, \sum_{j=0}^{t-1}\frac{g(x,y)*p_{ij}}{\omega_1}\right]^T \quad (14)$$

and saved into the vector:

$$\mu_T = [\mu_{00}, \mu_{01}, \mu_{10}, \mu_{11}]^T \quad (15)$$

Finally, the desired threshold vector $[s, t]$ is selected by maximizing the trace of inter class matrix as follows:

$$S_b = \sum_{k=0}^{1}\frac{\omega_k*(\mu_k - \mu_T)^2}{\omega_0*(1-\omega_0)} \quad (16)$$

C. Feature Extraction

Feature extraction is one of the most crucial steps for osteoporosis recognition from the mandible CBCT image. Hence, an extra care was taken to look for the most important trabecular bone texture features that can assist the investigation of the under study classification. To describe the mandible CBCT image's texture properties, Tamura [24] suggested six different texture properties: Coarseness, Contrast, Directionality, Line-Likeness, Regularity, and Roughness. In most cases, the first three features are used because these features capture the high-level attributes of a texture and are also useful for the browsing of images [25].

1) Trabecular Bone Texture Features

The important structure parameters to be measured in this part include seven parameters namely trabecular nodes, trabecular termini, and trabecular separation, trabecular spacing, trabecular number, trabecular thickness, and bone volume ratio [26]. Some of these features are illustrated in Figure 7.

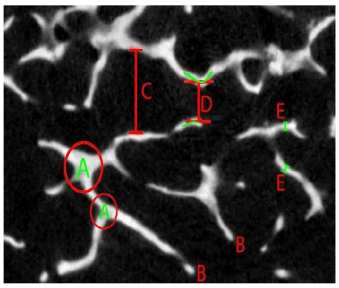

Fig. 7. Bone structure parameters. (A) Trabecular nodes, (B) trabecular termini, (C) trabecular separation, (D) trabecular spacing, and (E) trabecular thickness.

The seven criteria shown in the qualitative comparison for the trabecular bone structure between normal and osteoporotic bone are shown in Table I.

TABLE I. NORMAL AND OSTEOPOROTIC BONE COMPARISON

	Features	Normal	Osteoporotic
$\mathbf{P_1}$	Trabecular nodes (Tb.Nd)	High	Low
$\mathbf{P_2}$	Trabecular termini (Tb.Tm)	Low	High
$\mathbf{P_3}$	Trabecular separation (Tb.Sp)	Low	High
$\mathbf{P_4}$	Trabecular spacing (Tb.Sc)	Low	High
$\mathbf{P_5}$	Trabecular number (Tb.N)	High	Low
$\mathbf{P_6}$	Trabecular thickness (Tb.Th)	High	Low
$\mathbf{P_7}$	Bone volume over total volume (BV/TV)	High	Low

2) Hybrid Feature of Tamura Texture based Extraction Method

Coarseness, contrast, direction, number of non-zero pixels, length of edges, number of edges, and mean edge length, are good indicators of the bone parameters mentioned above. If the bone has a low Tb.Nd, Tb.N, Tb.Th, and BV/TV and high Tb.Tm, Tb.Sp and Tb.Sc then coarseness, contrast, direction, length of edges, and mean edge length will be high and the number of non-zero pixels and the number of edges will be low, which is an evidence of osteoporosis presence. If the bone has high Tb.Nd, Tb.N, Tb.Th, and BV/TV and high Tb.Tm, Tb.Sp and Tb.Sc then coarseness, contrast, direction, length of edges and mean edge length will be low, the non-zero pixels and the number of edges will be high which means a normal bone case. Coarseness, contrast and direction are evaluated by applying the extension of Tamura texture features for 3D images [27]. The 3D Tamura includes coarseness, contrast, and direction.

a) 3D Tamura Coarseness

Its computation follows the same steps as in the 2D case, but another dimension is added to the first step, for each point (x, y, z), as in (17):

$$Al(x,y,z) = \frac{1}{2^{3l}}\sum_{i=x-m}^{x+m-1}\left(\sum_{j=y-m}^{y+m-1} f(x,y,z)\right) \quad (17)$$

where $m=2^{e-1}$ and e determines the size of the neighborhood, that is $2^l \times 2^l \times 2^l$.

This part of the algorithm depends on the size of particular images. In the second step of computing 3D Tamura coarseness, take the differences by the same way as in 2D case but for three directions instead of two, calculated by the equations 18, 19, and 20 for the *x*-axis, *y*-axis, and *z*-axis, respectively.

$$E_{l,h} = |A_l(x + 2^{l-1}, y, z) - A_l(x - 2^{l-1}, y, z)| \quad (18)$$

$$E_{l,v} = |A_l(x, y + 2^{l-1}, z) - A_l(x, y - 2^{l-1}, z)| \quad (19)$$

$$E_{l,z} = |A_l(x, y, z + 2^{l-1}) - A_l(x, y, z - 2^{l-1})| \quad (20)$$

b) 3D Tamura Contrast

The algorithm for contrast is applicable on images of any dimensionality, and the feature from Tamura's set can be derived in the 2D case by simply adding another dimension. Tamura contrast in 3D is used in the same way as it was presented for the 2D case.

c) 3D Tamura Directionality

3D Tamura directionality cannot be derived straight forwardly in the 2D case. First, it is needed to form convolution kernels to compute the derivation in three directions along the three axes as shown in Figure 8.

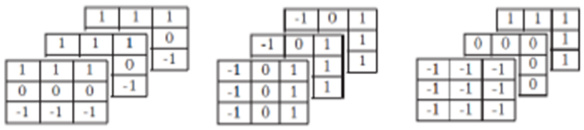

(a) (b) (c)

Fig. 8. Convolution kernels (a) kernel *X*, (b) kernel *Y*, and (c) kernel *Z*.

These kernels are used to create derivatives in the *x*-axis (ΔX), *y*-axis (ΔY), and *z*-axis (ΔZ) by convolution with the input image. Then following are calculated:

$$\theta_1 = \tan^{-1}\frac{\Delta_Y}{\Delta_X} + \frac{\pi}{2} \quad (21)$$

$$\theta_2 = \tan^{-1}\frac{\Delta_Z}{\Delta_Y} + \frac{\pi}{2} \quad (22)$$

$$\theta_3 = tan^{-1}\frac{\Delta_X}{\Delta_Z} + \frac{\pi}{2} \quad (23)$$

Then the 16 bin histogram is created with each of *n* values, where $n \in <1, 2, 3>$. Then the final result is acquired in the same way as in the 2D case. Four more parameters were suggested and calculated by the authors, namely the number of non-zero pixels, the length of the edges, the number of the edges, and the mean edge length. These features will be used as the input parameters for the ANN classifier, whose output would classify the patient as having osteoporosis or not. The ANN will be trained according to the steps described below.

D. The BP-NN Classifier

Many methods such as K-Nearest Neighbor (KNN), Support Vector Machine (SVM), or ANNs can be used for classification. In this work, an ANN will be implemented as the classifier with back propagation training algorithm based on the deepest-descent technique. The applied ANN is able to minimize the error of nonlinear functions of high complexity, and is provided with a suitable number of hidden units [28].

1) The Proposed Diagnosis Model

A feed-forward Back Propagation ANN (BPANN) is proposed to perform the classification for the diagnosis of osteoporosis. The BPANN consists of three layers: an input layer, one hidden layer, and an output layer. Fifteen hidden layer neurons are created and trained. The input and target samples are randomly chosen and automatically divided into 60% for training, 40% for validation and test sets. Sigmoid signal is selected as the activation function. The sigmoid function is a non-linear S-shaped curve function which is suitable for classification problems. It is a strictly increasing function. The input layer neuron number is determined by the number of features selected. The input neurons correspond to the seven input features (P_1 to P_7 of Table I). The number of neurons of the output layer is determined by the number of expected targets, which can take only two values in the proposed work, namely either 1 or 0 corresponding to the osteoporosis test which can be either positive or negative. The number of hidden neurons is determined by the Hecht-Nielsen theorem [29] which states that any continuous function can be represented by a neural network that has only one hidden layer with exactly $2n+1$ nodes, where n is the number of input nodes. The proposed ANN is shown in Figure 9.

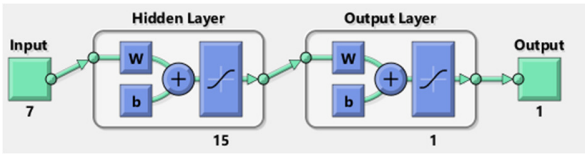

Fig. 9. Architecture of the BPANN (7:15:1)

2) Learning Methods of the BPANN

Supervised learning is implemented during the learning process. In this process, the expected output is already presented to the network. The collected data, in which the patient is already known as either an osteoporosis case or not are divided into two groups, one is used for training the ANN and the other is used for testing the trained network [30]. MATLAB is used as the computation tool for the training and implementation of the classification phase. The summary of the network components and parameters for the ANN classifier are listed in Table II.

TABLE II. ARCHITECTURE AND PARAMETERS OF THE ANN

Architecture (BPANN classifier)	
Number of input neurons, *n*	7
Number of hidden layers	1
Number of neurons in hidden layer, *m*	15
Number of output layer neurons	1
Activation function	Sigmoid
Learning method (rule)	Back-propagation
Learning rate, α	0.1
Number of iterations (epochs)	32
Measurements	Cross-Entropy

III. EXPERIMENTAL RESULTS

The extracted feature names and meanings for the involved data in the experiment for the mandible CBCT images that are practically used in the experimentation on the proposed scheme are shown in Table III.

TABLE III. DEFINITIONS OF THE USED INPUT VARIABLES

Input parameter	Feature
P_1	Coarseness
P_2	Contrast
P_3	Direction
P_4	Number of edge pixels
P_5	Length of edges
P_6	Number of edges
P_7	Mean edge length

The proposed method has been implemented using MATLAB 2018b. The database contains 120 CBCT images, organized in two classes, each consisting of 60 images, Normal and Osteoporotic. Seventy two images were used for training and 48 were used for testing. Table IV is the confusion matrix for the proposed BPANN classifier.

TABLE IV. CONFUSION MATRIX FOR CLASSIFICATION

N=48	Prediction: Healthy	Prediction: Osteoporotic	Total
Actual: Healthy	TN=23	FP=1	24
Actual: Osteoporotic	FN=0	TP=24	24
Total no. of images	23	25	48

TN: True Negative, FN: False Negative, TP: True Positive, and FP: False Positive

To evaluate the performance of the classifier, basically three metrics can be used, namely precision, recall, and accuracy. These measures are defined below.

$$\text{Accuracy} = \frac{\text{Number of Correctly Classified T.sting Samples}}{\text{Total Number of Testing Samples}} \quad (24)$$

$$\text{Precision} = \frac{\text{NTrue positives}}{\text{TTrue positives+False positives}} 0 \leq P \leq 1 \quad (25)$$

$$\text{Recall} = \frac{\text{NTrue positives}}{\text{TTrue positives+ False negatives}} 0 \leq R \leq 1 \quad (26)$$

Evaluating accuracy, precision, recall, and F1-score for the BPANN classifier using the above equations resulted in the values summarized in Table V. The classifier converged in 35 epochs.

TABLE V. BPANN CLASSIFIER PERFORMANCE

Testing sample percentage	Accuracy (A)	Precision (P)	Recall (R)	F1-score
40% from the dataset.	97.917%	0.96	1	0.97959

Applying the ANN to distinguish between healthy and osteoporotic persons resulted to almost 98% successful classification rate of the testing set. Table VI lists the training state values (the cross entropy) as a function of the number of iterations. These state values are clearly shown in Figure 10, which shows that the best validation performance occurs at 2.8548e-007 at epoch 35, which is the lowest possible value in our calculations using MATLAB.

TABLE VI. CROSS-ENTROPY VALUES FOR NUMBER OF EPOCHS

Number of epochs	Training	Validation	Testing
5	0.03862	0.02563	0.03862
10	0.005012	0.001818	0.003238
15	0.0007033	0.0002521	0.0004626
20	9554e-05	2.27e-05	6.118e-05
25	1.294e-05	3.229e-06	7.279e-05
30	1.853e-06	3.601e-07	1.169e-06
35	9e-09	5.576e-08	9e-09

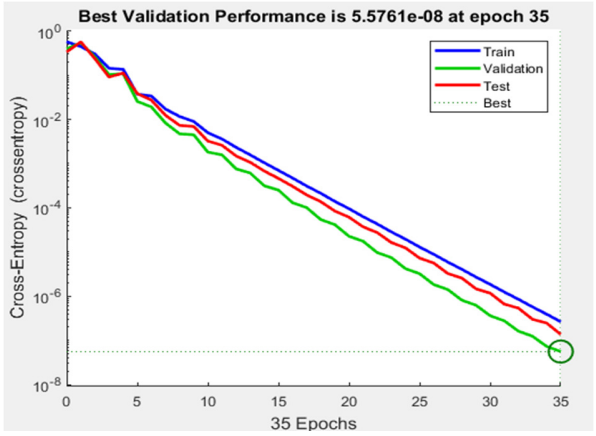

Fig. 10. Cross-entropy calculation as a function of the number of epochs.

IV. CONCLUSION

As CBCT images are inevitably used by dentists to evaluate the bone adequacy for dental implants, the proposed algorithm is designed to utilize the mandible trabecular bone properties found in these images for the early detection of osteoporosis. The experimental data set consists of 120 CBCT image slices obtained anonymously from local CBCT radiology centers. The performance of the suggested feed forward BPANN classifier was measured by precision, recall, and accuracy which were 0.96, 1, and 97.917%, respectively. It is worth mentioning that with the help of the proposed scheme, dentists will be able to predict osteoporosis accurately and efficiently. This would aid the effort of reducing the risk of jaw fracture and dental implant failure as well as reduce the cost of DEXA examination, medicines, and patient inconvenience. The scheme can be modified or improved in many ways. Improvements may be achieved through the acquisition of an algorithm that can be used to estimate the degree of osteoporosis, and an algorithm that can be used to unify the efforts for producing homogeneous and matched features when CBCT images of different sources and specifications are used.

REFERENCES

[1] E. Gungor, D. Yıldırım, and R. Cevik, "Evaluation of osteoporosis in jaw bones using cone beam CT and dual-energy X-ray absorptiometry," *Journal of Oral Science*, vol. 58, no. 2, pp. 185–194, Jun. 2016, doi: 10.2334/josnusd.15-0609.

[2] T. Link, "Osteoporosis Imaging: State of the Art and Advanced Imaging," *Radiology*, vol. 263, no. 1, pp. 3–17, Apr. 2012, doi: 10.1148/radiol.12110462.

[3] F. Esmaeli, S. Payahoo, M. Mobasseri, M. Johari, and J. Yazdani, "Efficacy of radiographic density values of the first and second cervical vertebrae recorded by CBCT technique to identify patients with osteoporosis and osteopenia," *Journal of Dental Research, Dental*

Clinics, Dental Prospects, vol. 11, no. 3, pp. 189–194, Jul. 2017, doi: 10.15171/joddd.2017.034.

[4] I. Barngkgei, I. Haffar, and R. Khattab, "Osteoporosis prediction from the mandible using cone-beam computed tomography," *Imaging science in dentistry*, vol. 44, no. 4, pp. 263–271, Dec. 2014, doi: 10.5624/isd.2014.44.4.263.

[5] E. Klintstrom, *Image Analysis for Trabecular Bone Properties on Cone-Beam CT Data*. Linkoping, Sverige: Linkoping University Electronic Press, 2017.

[6] Y. Hua, O. Nackaerts, J. Duyck, F. Maes, and R. Jacobs, "Bone quality assessment based on cone beam computed tomography imaging," *Clinical oral implants research*, vol. 20, no. 8, pp. 767–771, Mar. 2009, doi: 10.1111/j.1600-0501.2008.01677.x.

[7] Y. Liu *et al.*, "Calibration of cone beam CT using relative attenuation ratio for quantitative assessment of bone density: A small animal study," *International journal of computer assisted radiology and surgery*, vol. 8, no. 5, pp. 733–739, Dec. 2012, doi: 10.1007/s11548-012-0803-5.

[8] D. Kannan, L. Bijai Kumar, and P. Subiksha, "Cone Beam Computed Tomography Evaluation of Postmenopausal Alveolar Bone Changes in Osteoporotic Women," *International Journal of Oral Implantology & Clinical Research*, vol. 6, no. 3, pp. 65–68, Sep. 2014, doi: 10.5005/jp-journals-10012-1138.

[9] I. Barngkgei, E. Joury, and A. Jawad, "An Innovative Approach In Osteoporosis Opportunistic Screening By The Dental Practitioner: The Use Of Cervical Vertebrae And Cone Beam Computed Tomography With Its Viewer Program," *Oral Surgery, Oral Medicine, Oral Pathology, Oral Radiology*, vol. 120, no. 5, pp. 651–659, Aug. 2015, doi: 10.1016/j.oooo.2015.08.008.

[10] M. B. Alonso, T. Vasconcelos, L. Lopes, P. Watanabe, and D. Freitas, "Validation of cone-beam computed tomography as a predictor of osteoporosis using the Klemetti classification," *Brazilian Oral Research*, vol. 30, no. 1, pp. 1–8, May 2016, doi: 10.1590/1807-3107BOR-2016.vol30.0073.

[11] Suprijanto, Azhari, E. Juliastuti, A. Septyvergy, and N. Setyagar, "Dental panoramic image analysis for enhancement biomarker of mandibular condyle for osteoporosis early detection," *Journal of Physics: Conference Series*, vol. 694, no. 1, Mar. 2016, Art no. 012066, doi: 10.1088/1742-6596/694/1/012066.

[12] R. Mostafa, E. Arnout, and M. M. A. El-Fotouh, "Feasibility of Cone Beam Computed Tomography Radiomorphometric Analysis and Fractal Dimension in Assessment of Postmenopausal Osteoporosis in Correlation with Dual X-ray Absorptiometry," *Dento maxillo facial radiology*, vol. 45, no. 7, Jul. 2016, Art no. 20160212, doi: 10.1259/dmfr.20160212.

[13] E. Gungor, O. S. Aglarci, M. Unal, M. S. Dogan, and S. Guven, "Evaluation of mental foramen location in the 10-70 years age range using cone-beam computed tomography," *Nigerian Journal of Clinical Practice*, vol. 20, no. 1, pp. 88–92, Jan. 2017, doi: 10.4103/1119-3077.178915.

[14] M. Alkhader, A. Aldawoodyeh, and N. Abdo, "Usefulness of measuring bone density of mandibular condyle in patients at risk of osteoporosis: A cone beam computed tomography study," *European Journal of Dentistry*, vol. 12, no. 3, pp. 363–368, Aug. 2018, doi: 10.4103/ejd.ejd_272_17.

[15] N. Shameena and R. Jabbar, "A Study of Preprocessing and Segmentation Techniques on Cardiac Medical Images," *International Journal of Engineering Research & Technology (IJERT)*, vol. 3, no. 4, pp. 336–341, Apr. 2014.

[16] T. Acharya and A. K. Ray, *Image Processing: Principles and Applications*. Hoboken, New Jersey: John Wiley & Sons, 2005.

[17] Y.-T. Kim, "Contrast enhancement using brightness preserving bi-histogram equalization," *IEEE Transactions on Consumer Electronics*, vol. 43, no. 1, pp. 1–8, Feb. 1997, doi: 10.1109/30.580378.

[18] P. Scheunders, "A multivalued image wavelet representation based on multiscale fundamental forms," *IEEE Transactions on Image Processing*, vol. 11, no. 5, pp. 568–575, May 2002, doi: 10.1109/TIP.2002.1006403.

[19] W. Ma, J. Morel, S. Osher, and A. Chien, "An L1-based variational model for Retinex theory and its application to medical images," in *CVPR 2011*, Providence, RI, USA, Jun. 2011, pp. 153–160, doi: 10.1109/CVPR.2011.5995422.

[20] E. H. Land, "Recent advances in retinex theory," *Vision Research*, vol. 26, no. 1, pp. 7–21, Jan. 1986, doi: 10.1016/0042-6989(86)90067-2.

[21] L. Ding and A. Goshtasby, "On the Canny edge detector," *Pattern Recognition*, vol. 34, no. 3, pp. 721–725, Mar. 2001, doi: 10.1016/S0031-3203(00)00023-6.

[22] R. Muthukrishnan and R. Radha, "Edge detection techniques for image segmentation," *International Journal of Computer Science & Information Technology*, vol. 3, no. 6, pp. 259–267, 2011.

[23] J. Zhang and J. Hu, "Image Segmentation Based on 2D Otsu Method with Histogram Analysis," in *International Conference on Computer Science and Software Engineering*, Hubei, China, Dec. 2008, vol. 6, pp. 105–108, doi: 10.1109/CSSE.2008.206.

[24] H. Tamura, S. Mori, and T. Yamawaki, "Textural Features Corresponding to Visual Perception," *IEEE Transactions on Systems, Man, and Cybernetics*, vol. 8, no. 6, pp. 460–473, Jun. 1978, doi: 10.1109/TSMC.1978.4309999.

[25] N. Bagri and P. Johari, "A Comparative Study on Feature Extraction using Texture and Shape for Content Based Image Retrieval," *International Journal of Advanced Science and Technology*, vol. 80, no. 4, pp. 41–52, Jul. 2015, doi: 10.14257/ijast.2015.80.04.

[26] B. Klintström, E. Klintström, O. Smedby, and R. Moreno, "Feature Space Clustering for Trabecular Bone Segmentation," presented at the Image Analysis: 20th Scandinavian Conference, SCIA 2017, Tromso, Norway, Jun. 2017, pp. 65–75, doi: 10.1007/978-3-319-59129-2_6.

[27] T. Majtner and D. Svoboda, "Extension of Tamura Texture Features for 3D Fluorescence Microscopy," in *Second International Conference on 3D Imaging, Modeling, Processing, Visualization & Transmission*, Zurich, Switzerland, Oct. 2012, pp. 301–307, doi: 10.1109/3DIMPVT.2012.61.

[28] B. R. Kowalski and C. Bender, "k-Nearest Neighbor Classification Rule (pattern recognition) applied to nuclear magnetic resonance spectral interpretation," *Analytical Chemistry*, vol. 44, no. 8, pp. 1405–1411, 1972.

[29] R. Hecht-Nielsen, "Kolmogorov's Mapping Neural Network Existence Theorem," presented at the First International Conference on Neural Networks, San Diego, CA, USA, 1987, pp. 11–13.

[30] C. Peterson, T. Rognvaldsson, and L. Lonnblad, "JETNET 3.0—A versatile artificial neural network package," *Computer Physics Communications*, vol. 81, no. 1–2, pp. 185–220, Jun. 1994, doi: 10.1016/0010-4655(94)90120-1.